LETTER

Atomic structure of anthrax protective antigen pore elucidates toxin translocation

Jiansen Jiang[1,2], Bradley L. Pentelute[3], R. John Collier[4] & Z. Hong Zhou[1,2]

Anthrax toxin, comprising protective antigen, lethal factor, and oedema factor, is the major virulence factor of *Bacillus anthracis*, an agent that causes high mortality in humans and animals. Protective antigen forms oligomeric prepores that undergo conversion to membrane-spanning pores by endosomal acidification, and these pores translocate the enzymes lethal factor and oedema factor into the cytosol of target cells[1]. Protective antigen is not only a vaccine component and therapeutic target for anthrax infections but also an excellent model system for understanding the mechanism of protein translocation. On the basis of biochemical and electrophysiological results, researchers have proposed that a phi (Φ)-clamp composed of phenylalanine (Phe)427 residues of protective antigen catalyses protein translocation via a charge-state-dependent Brownian ratchet[2–9]. Although atomic structures of protective antigen prepores are available[10–14], how protective antigen senses low pH, converts to active pore, and translocates lethal factor and oedema factor are not well defined without an atomic model of its pore. Here, by cryo-electron microscopy with direct electron counting, we determine the protective antigen pore structure at 2.9-Å resolution. The structure reveals the long-sought-after catalytic Φ-clamp and the membrane-spanning translocation channel, and supports the Brownian ratchet model for protein translocation. Comparisons of four structures reveal conformational changes in prepore to pore conversion that support a multi-step mechanism by which low pH is sensed and the membrane-spanning channel is formed.

Triggering conversion from protective antigen (PA) prepore to pore by *in vitro* acidification leads to rapid and irreversible aggregation. Attempts to prevent aggregation by screening detergents have largely failed[15]. By low-pH treatment of PA prepores directly on electron microscopy (EM) grids containing a thin layer of continuous carbon film, we obtained dispersed particles of PA pore without aggregation (Extended Data Fig. 1). We then acquired drift-corrected cryo-electron microscopy (cryoEM) images (Extended Data Fig. 1b–d) and reconstructed a map at an overall resolution of 2.9 Å using 60,455 particles (Fig. 1, Extended Data Fig. 2 and Supplementary Video 1). The resolution for most regions of the cryoEM map is ~2.8 Å (Extended Data Fig. 2c). Our map reveals rich high-resolution structural features, including amino-acid side chains and 14 chelated Ca^{2+} ions (Extended Data Fig. 1e–h), and has allowed unambiguous *de novo* atomic modelling (Extended Data Table 1) and detailed structure and function analyses.

The overall structure of the PA pore has a 'flower-on-a-stem' architecture, including corolla, calyx, and stem from top to bottom (Figs 1b and 2a and Supplementary Video 1). Each PA protomer is divided into four domains in the PA prepore[10], named 1′, 2, 3, and 4. In the PA pore, domains 1′, 3, and 4 form the corolla and domain 2 forms the calyx and the stem; therefore we designate the parts of domain 2 corresponding to the calyx and the stem as 2c (residues 259–274 and 354–487) and 2s (residues 275–353), respectively (Fig. 2b, c). Domains 1′ and 2c form a compact structure responsible for substrate protein binding and intake (Fig. 2). Domain 2s is an extended β-hairpin ($2\beta_{2s}$ and $2\beta_{3s}$), seven

copies of which assemble to form a membrane-spanning 14-stranded β-barrel 105 Å in length and 27 Å (from C_α to C_α) in diameter (Fig. 2). Domain 3 is located peripherally and has close contact with domains 1′ and 2c (Fig. 2b). The cryoEM density of domain 4 is weak and has the lowest resolution among all domains (inset of Fig. 1b and Extended Data Fig. 2c), probably because of its flexibility from minimal contact with the other domains. Rigid-body fitting of domain 4 of the PA prepore crystal structure to the cryoEM map shows domain 4 shifts ~4 Å towards the central axis in the PA pore (Extended Data Fig. 3).

The translocation channel of the PA pore has a funnel shape and can be divided into four parts based on diameters calculated with MOLE[16]: mouth, Φ-clamp, throat, and tube (Fig. 3a, b). Its surface is negatively charged and mainly hydrophilic, but hydrophobic patches are seen at the α-clamp[14] of the mouth, near the Φ-clamp, and at the middle of the tube (Fig. 3a, c). As proposed on the basis of the PA prepore structure[10], the negatively charged surface promotes passage of cations, and the hydrophilic surface facilitates passage of substrate proteins/polypeptides.

The mouth has a 30-Å opening and inner diameters varying down to 20 Å (Fig. 3a); it can accommodate protein secondary structure elements, but not folded domains such as the amino (N)-terminal of lethal factor (LF_N). The Φ-clamp below the mouth becomes the bottleneck of the entire channel, with a solvent-excluded inner diameter of only 6 Å (Fig. 3a, b), which is smaller than protein secondary structure elements and therefore may only allow passage of fully unfolded polypeptides. Underneath the Φ-clamp are the throat, which is an enlarged (~18 Å) bulb-shaped chamber, and the tube formed by the 14-stranded β-barrel with inner diameters in the range 12–18 Å and rich in Ser and Thr residues in its middle region (Fig. 3a, b). The large diameter (>12 Å) of
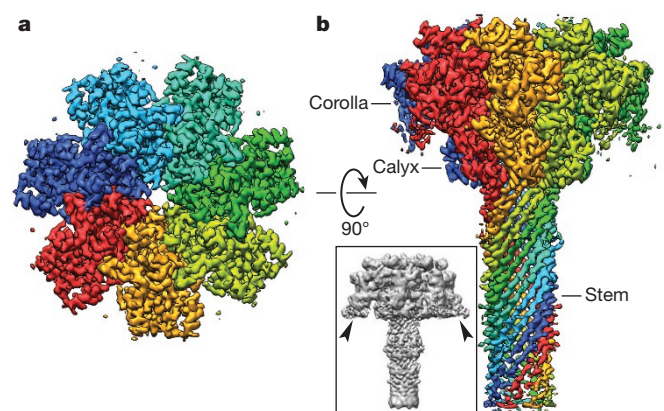

Figure 1 | CryoEM reconstruction of the PA pore. a, b, Surface representations of the cryoEM map of the PA pore at 2.9-Å resolution as viewed from the top (**a**) and the side (**b**). Individual protomers of PA heptamer are colour-coded. Inset of **b** shows the unsharpened cryoEM map in which the flexible domains 4 (arrowheads) are visible.

[1]Department of Microbiology, Immunology and Molecular Genetics, University of California, Los Angeles, California 90095, USA. [2]California NanoSystems Institute, University of California, Los Angeles, California 90095, USA. [3]Department of Chemistry, Massachusetts Institute of Technology, Cambridge, Massachusetts 02139, USA. [4]Department of Microbiology and Immunobiology, Harvard Medical School, Boston, Massachusetts 02115, USA.
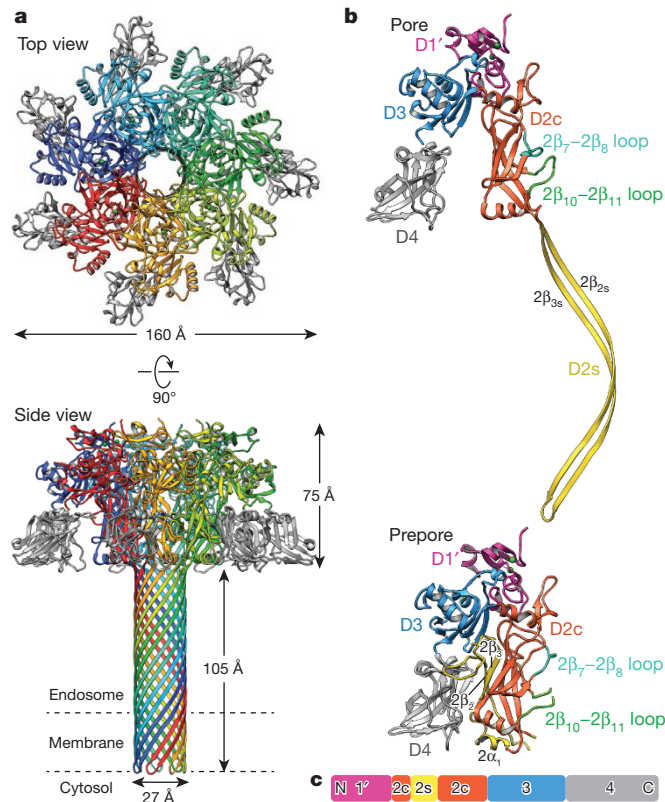
Figure 2 | Atomic model of the PA pore. a, Top and side views of the atomic model of the PA pore shown as ribbons. Protomers are colour-coded except for domain 4 (grey). **b**, Structural comparison of the protomers of the PA pore and prepore (PDB accession number 1TZO). The domains are coloured differently according to **c**. **c**, Domain organization of the PA protomer.

Figure 3 | Translocation channel of the PA pore. a, Electrostatic surface (left) and channel radius profile (right) of the PA pore. An α-helix (green surface model of residues 555–574 of lethal factor; PDB accession number 1J7N) is modelled in the β-barrel. The green arrow depicts the direction of protein translocation. Colour scale, kcal (mol e)$^{-1}$. **b**, The translocation channel (dots) running through the Φ-clamp. Two protomers of the PA pore are shown as ribbons. Residues Glu398, Asp425, Asp426, Phe427, and Ser429 (ball-and-stick) are exposed to the channel. **c, d**, Hydropathy surface of the PA pore (brown: hydrophobic; purple: hydrophilic; white: neutral). In **c**, the front half of the structure is removed to show the luminal surface. In **d**, two 1,2-dihexadecanoyl-sn-glycero-3-phosphocholine (DPPC) lipid molecules are modelled near the membrane insertion region. **e**, Bottom and side views of the segmented cryoEM map showing the β-barrel (yellow) bound with disordered detergent molecules (grey). **f**, The 14-stranded β-barrel (ribbons) and the hydrophobic residues (spheres) on its outer surface. The hydrophobic residues are depicted on different protomers for the ease of presentation.

the throat and tube can accommodate an α-helix which may be formed by polypeptides after passing the Φ-clamp (Fig. 3a). The diameter and the hydrophilic property of this part of channel are similar to those of the exit tunnel of the ribosome, which is proposed to translocate α-helices[17,18].

The mouth and the tube are the only two openings of the channel, and are accessible to the endosomal and cytosolic compartments, respectively (Fig. 3a). The rest of the channel is 'water-tight' and without holes permeable to small molecules. The substrate protein blocks the small hole of the Φ-clamp before or during translocation[2]. Thus the Φ-clamp may act as a gate separating the endosomal and cytosolic compartments. The differences of proton concentration (ΔpH) and electrical potential (Δψ) across the Φ-clamp (Fig. 3a) may serve as the primary driving force for substrate protein translocation[3].

In contrast to the hydrophilic inner surface of the β-barrel, its outer surface is largely hydrophobic (Fig. 3c, d). The Phe residues (313, 314, and 324) form two aromatic belts on opposite sides of the lipid bilayer (Fig. 3d), which may stabilize membrane insertion[19,20]. The cryoEM map shows that the transmembrane region is surrounded by a cloud of disordered densities, which we interpret as bound detergent molecules that were added during sample preparation (Fig. 3e). Surprisingly, an additional hydrophobic surface in the middle of the β-barrel containing a cluster of hydrophobic residues (Ile289, Val332, Ile334, Leu338 and Leu340 from each protomer) was also bound with detergent molecules (Fig. 3d–f). However, the function of this additional hydrophobic region is unknown.

The overall architecture of the PA pore is similar to those of bacterial toxins α-haemolysin and *Vibrio cholerae* cytolysin in their membrane-inserted conformations (Extended Data Fig. 4) despite differences in functions[21,22]. The β-barrel of the PA pore is twice as long as those of the other two toxins and may facilitate LF and oedema factor translocation by entropically stabilizing an α-helix within the confinement of
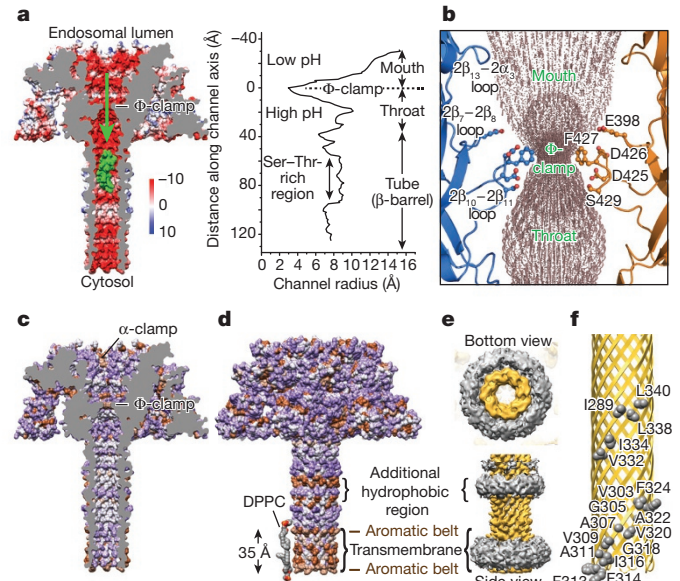
the cylindrical channel[9,17]. This longer barrel may also be necessary to accommodate its receptor situated between domain 4 and the host membrane[11] (Extended Data Fig. 4). Except for this length difference, the 14-stranded β-barrels of the PA pore, α-haemolysin, and *V. cholerae* cytolysin share geometries, such as diameter, twist of β-strands, and pitch length (Extended Data Fig. 4).

In the PA pore, the seven $2\beta_{10}$–$2\beta_{11}$ loops of the heptamer converge to form an iris with a 6-Å hole bounded by a symmetrical arrangement of the seven Phe427 residues (Fig. 4). By contrast, these loops in the PA prepore do not engage each other[10,12], but circumscribe a 30-Å central hole with adjacent Phe427 residues spaced ∼14 Å apart (Extended Data Fig. 5a). In the PA pore, each $2\beta_{10}$–$2\beta_{11}$ loop is stabilized by close interactions with the $2\beta_7$–$2\beta_8$ loop of the same protomer and the $2\beta_{10}$–$2\beta_{11}$ loops of its two neighbouring protomers. The hydrogen bonds between Asn399 and Ser428 and between Asn399 and Lys397' of an adjacent protomer form a chain of interactions, which give rise to a ring of loops at the iris inside the PA pore (Extended Data Fig. 5b). Consistently, mutation of Ser428 abolished protein translocation, and mutation of Lys397 or Asn399 resulted in a dominant negative effect[23–25]. In the PA homologues found in *Clostridium* species, Lys397 and Asp426 are both replaced by uncharged Gln[26], implying that this chain of interactions might be formed differently in these homologues.

The aryl plane of Phe427 from each protomer is parallel to the central axis of the PA pore. Neighbouring Phe427 residues interact with each other by aromatic CH–π interaction in a tilted T-shaped configuration[27] and possibly by hydrophobic interaction, thus forming the Φ-clamp (Fig. 4 and Extended Data Fig. 5). The integrity of the Φ-clamp is required for catalysis of protein translocation, as mutation of even a single Phe427
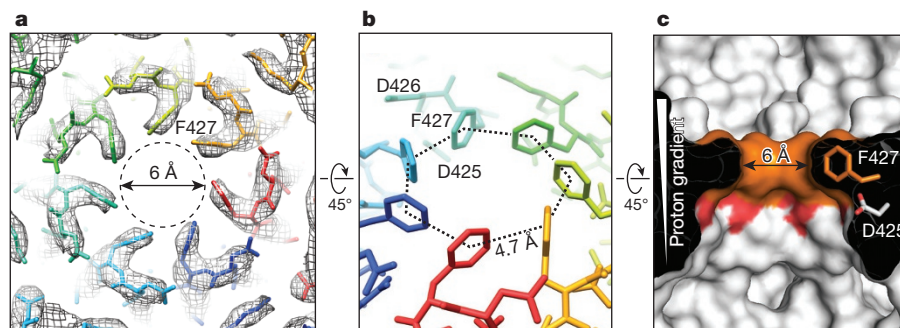
Figure 4 | Structure of the Φ-clamp. **a**, Top view of the Φ-clamp region of the PA pore showing the cryoEM map (mesh) superimposed with the atomic model (stick). **b**, Tilted view of the Φ-clamp with seven protomers coloured differently, showing the aromatic CH–π interaction. **c**, Cross-section side view of the translocation channel near the Φ-clamp region. The Φ-clamp (Phe427) and the conserved acidic residue Asp425 are coloured in orange and red, respectively.

residue of the Φ-clamp severely reduced translocation efficiency and disrupted the seal against cation passage[5]. Because the PA pore translocates polypeptides with various side chains, the Φ-clamp may act like an elastic 'O-ring', changing its size and shape to allow an unhindered passage of different amino-acid residues while maintaining a good seal during translocation. In the recently reported structure of bacterial amyloid secretion channel CsgG, eight Phe residues form a Φ-clamp, which differs from that in the PA pore in having a 9.5-Å hole and facilitating protein translocation in an ungated manner[28].

Evidence from electrophysiological studies indicates that the proton gradient across the endosomal membrane is the primary driving force for unidirectional translocation of proteins through the PA pore[3]. Proton-driven transporters usually involve protonation-dependent conformational changes of two or more alternating gates. In the PA pore, however, there is only one gate, namely the Φ-clamp, and neither the Φ-clamp nor its nearby residues probably undergo a protonation-dependent conformational change. Indeed, the PA pore structure supports the charge-state-dependent Brownian ratchet model[2–9], proposed earlier. In this model, a negative electrostatic barrier within the pore hinders the passage, by Brownian motion, of deprotonated acidic residues[3,4,29]. The fact that acidic residues in the acidic environment

of the endosome have a higher probability of being protonated, and are thus free to pass the barrier, than those in the neutral environment of the cytosol, leads necessarily to unidirectional movement of polypeptides across the barrier. Consistent with this model, the PA pore structure shows three acidic residues, Asp425, Asp426, and Glu398, to be near the Φ-clamp and proximal to the pore axis (Fig. 3b), generating a strong negative electrostatic barrier demarcating the endosomal and cytosolic compartments. In addition, the highly conserved acidic residue Asp425 located directly underneath the Φ-clamp is ideally positioned as a proton sink that may strip off protons from protonated acidic residues passing the Φ-clamp (Fig. 4c). Besides the charge barrier in the Φ-clamp, efficient protein translocation may require additional charged spots, such as the top region of the β-barrel[8].

A key question about the low-pH-triggered conversion from prepore to pore is how PA senses pH. A notable conformational change during the conversion is that the $2\beta_{10}$–$2\beta_{11}$ loop is flipped from one side to the other (Fig. 5a and Extended Data Fig. 6). Interestingly, this loop has different conformations in the two crystal structures of PA octameric prepores ($[PA_{63}]_8$, PDB accession number 3HVD; $[PA_{63}]_8[LF_N]_4$, PDB accession number 3KWV) whereas the remaining parts of the structures are largely unchanged[9,13,14]; that is, this loop is in the pore and
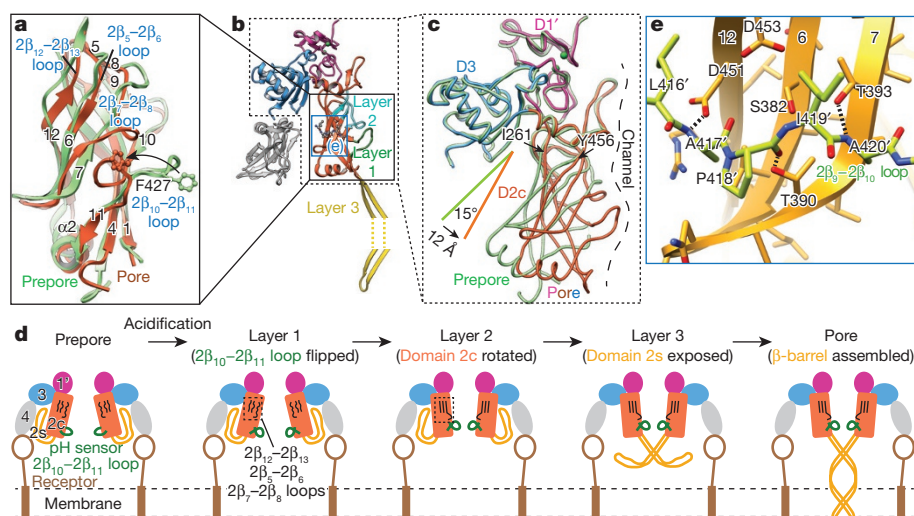

Figure 5 | Conversion from prepore to pore. **a**, Superimposition of domains 2c of the PA pore and prepore (monomer; PDB accession number 3TEW). Loops undergoing dramatic conformational changes during the prepore to pore conversion are labelled (blue). **b**, Overview of the three layers of conformational changes during the conversion. The interaction between the $2\beta_9$–$2\beta_{10}$ loop and the β-sheet (blue box) is shown in **e**. **c**, Superimposition of the PA pore (pink, orange, and blue; coloured by domain) and prepore (light green; PDB accession number 1TZO). Domains 4 and 2s are removed for clarity. Between the two structures, domain 2c has a Cα root-mean-square deviation = 6.87 Å, whereas domains 1′ and 3 remain unchanged with a Cα root-mean-square deviation = 0.54 Å and 0.58 Å, respectively. **d**, Illustration of the steps of conformational changes during the prepore to pore conversion. For simplicity, only two protomers are illustrated. **e**, Interface between the $2\beta_9$–$2\beta_{10}$ loop (green) and the bent β-sheet (gold) of $2\beta_{12}$, $2\beta_6$, and $2\beta_7$ of the adjacent protomer in the PA pore. Hydrogen bonds between the backbone of the loop and the side chains of the β-sheet are depicted with dashed lines.

prepore states in 3HVD (Extended Data Fig. 6b) and 3KWV, respectively. This comparison suggests that the $2\beta_{10}$–$2\beta_{11}$ loop can switch between two conformations without affecting the overall structure. Mutation of the conserved Asn422 or Asp425 in this loop abolished the prepore to pore conversion at low pH in a dominant negative manner[25]. Therefore we interpret this loop as a pH sensor. Surprisingly, this loop does not possess any His, a residue whose pK_a of approximately 6 falls in the pH range of 5–7 where the prepore to pore conversion occurs. The conformational change of this loop might result from destabilization and rearrangement of hydrogen bonds upon exposure to low pH, or alternatively from perturbed pK_a of Asp residues (425 and 426) in this loop. We note that other parts of PA might impact pH sensing. Prior work has shown mutation of residues near or in the $2\beta_2$–$2\beta_3$ loop, or at the domain 2/domain 4 interface, or deletion of the $2\beta_2$–$2\beta_3$ loop changed the pH threshold for conversion but did not abolish the low-pH sensitivity[25,30]. These observations suggest that the involved residues might regulate pH sensing.

We find that the prepore to pore conversion involves three layers of conformational changes, all located within domain 2 (Fig. 5b). The first layer is the above-mentioned pH-sensing $2\beta_{10}$–$2\beta_{11}$ loop. Low-pH-triggered conformational change of this loop is relayed to the following layers sequentially as detailed below.

The second layer involves the $2\beta_7$–$2\beta_8$, $2\beta_5$–$2\beta_6$, and $2\beta_{12}$–$2\beta_{13}$ loops, which are positioned in an anti-parallel manner (Fig. 5a). In the PA pore, the N-terminal half of the $2\beta_7$–$2\beta_8$ loop moves downwards to form a U-shaped turn tethered to the putative pH-sensing $2\beta_{10}$–$2\beta_{11}$ loop via a hydrogen bond between Asn399 and Ser428 (Fig. 5a and Extended Data Figs 5b and 6e). This new inter-loop interaction may relay the low-pH-triggered conformational changes from the first layer to the second layer as supported by the dominant negative effect of Asn399 or Lys397 mutation[24,25], which breaks the hydrogen bond network connecting these two loops (Extended Data Fig. 5b). As a result of the downward pull from the $2\beta_7$–$2\beta_8$ loop, all three loops of the second layer become straightened in the PA pore, with parts of the $2\beta_5$–$2\beta_6$ and $2\beta_{12}$–$2\beta_{13}$ loops forming strands to augment $2\beta_6$ and $2\beta_{12}$, respectively (Fig. 5a and Extended Data Fig. 6c, f). This conformational change is supported by the observation that mutating any of Pro379, Val455, and Asn458 of these loops led to defects in protein translocation[25]. This conformational change leads to the convergence of domain 2c of each protomer and formation of the Φ-clamp by a 15° rotation of domain 2c around the hinge residues Ile261 and Tyr456, with its distal edge moving for 12 Å towards the central axis of the PA pore (Fig. 5c and Supplementary Video 2). Indeed, tethering domain 2 to domain 4 by receptor binding or stabilizing the interface between these two domains by a poly-γ-D-glutamate capsule impeded domain convergence and therefore decreased the pH threshold required for the prepore to pore conversion[11,12,30]. Conversely, destabilizing the domain 2/domain 4 interface by point mutations increased the pH threshold[30].

The third layer, resulting from the second layer of conformational changes, involves release and refolding of the precursor of domain 2s (that is, $2\beta_2$, $2\beta_3$, $2\alpha_1$, and the membrane insertion loop), and leads to the formation of the membrane-spanning β-barrel (Figs 2 and 5b and Extended Data Fig. 7). The rotation of domain 2c opens the pocket between domain 2c and domain 4 to release the precursors of domain 2s, which then come together to form the β-barrel (see details in Extended Data Fig. 7b). The β-barrel formation might be the result, rather than the cause, of the convergence of domain 2c, as supported by a cryoEM map obtained from a subset of particles that shows converged domain 2c in the pore state but lacks the β-barrel (Extended Data Fig. 8). We note that the stability of the domain 2/domain 4 interface was found to be a rate-limiting barrier to the conversion[30] and the separation between domain 2c and domain 4 might also happen at an earlier stage of the conversion.

Taken together, these results suggest a multi-step mechanistic model of the low-pH-triggered conversion from prepore to pore (Fig. 5d). First, the $2\beta_{10}$–$2\beta_{11}$ loop as a pH sensor changes its conformation upon acidification (layer 1). Second, consequently, the $2\beta_7$–$2\beta_8$, $2\beta_5$–$2\beta_6$, and $2\beta_{12}$–$2\beta_{13}$ loops become ordered (layer 2), resulting in the convergence of domain 2c and the formation of the Φ-clamp. Last, as a result of the separation of domain 2c from domain 4, the precursors of domain 2s are released and refold into a uniform β-barrel (layer 3), which, as a final step, inserts into the endosomal membrane, ready for delivering the toxic enzymes into the cytosol.

In the PA pore, the convergence of domain 2c creates a large inter-protomer interface to stabilize the pore conformation (Extended Data Fig. 7a). Key to the formation of a functional PA pore is a newly identified interface between the $2\beta_9$–$2\beta_{10}$ loop of one protomer and the triple-stranded β-sheet ($2\beta_{12}$, $2\beta_6$, and $2\beta_7$) of its neighbour (Fig. 5e). The above-mentioned convergence of domain 2c brings them together to form a new binding interface primarily mediated by hydrogen bonds between the backbone of the loop and the side chains of Thr390, Thr393, and Asp451 of the β-sheet (Fig. 5e). These interactions explain the dominant negative effect of Ser382 or Thr393 mutant, the loss of PA activity of the Cys mutant of Thr390 or Asp451, and the conservation of Thr390 and Thr393 in PA homologues[25]. By contrast, these residues are accessible and free of interactions in the PA prepore, and thus might be potential drug targets for blocking the conversion to functional PA pores.

In summary, the 2.9-Å structure of the anthrax PA pore suggests the $2\beta_{10}$–$2\beta_{11}$ loop as a pH sensor to trigger conformational changes for prepore to pore conversion, supports a charge-state-dependent Brownian ratchet model of proton-driven protein translocation, and can inform efforts both to engineer PA to target cancer cells and to design measures to block anthrax toxin entering cells[14,21]. A more detailed mechanism of protein translocation through the PA pore awaits additional experimental evidence, such as structures of the PA pore in the act of polypeptide translocation.

1. Young, J. A. & Collier, R. J. Anthrax toxin: receptor binding, internalization, pore formation, and translocation. *Annu. Rev. Biochem.* **76,** 243–265 (2007).
2. Krantz, B. A. *et al.* A phenylalanine clamp catalyzes protein translocation through the anthrax toxin pore. *Science* **309,** 777–781 (2005).
3. Krantz, B. A., Finkelstein, A. & Collier, R. J. Protein translocation through the anthrax toxin transmembrane pore is driven by a proton gradient. *J. Mol. Biol.* **355,** 968–979 (2006).
4. Basilio, D., Juris, S. J., Collier, R. J. & Finkelstein, A. Evidence for a proton-protein symport mechanism in the anthrax toxin channel. *J. Gen. Physiol.* **133,** 307–314 (2009).
5. Janowiak, B. E., Fischer, A. & Collier, R. J. Effects of introducing a single charged residue into the phenylalanine clamp of multimeric anthrax protective antigen. *J. Biol. Chem.* **285,** 8130–8137 (2010).
6. Basilio, D., Jennings-Antipov, L. D., Jakes, K. S. & Finkelstein, A. Trapping a translocating protein within the anthrax toxin channel: implications for the secondary structure of permeating proteins. *J. Gen. Physiol.* **137,** 343–356 (2011).
7. Brown, M. J., Thoren, K. L. & Krantz, B. A. Charge requirements for proton gradient-driven translocation of anthrax toxin. *J. Biol. Chem.* **286,** 23189–23199 (2011).
8. Wynia-Smith, S. L., Brown, M. J., Chirichella, G., Kemalyan, G. & Krantz, B. A. Electrostatic ratchet in the protective antigen channel promotes anthrax toxin translocation. *J. Biol. Chem.* **287,** 43753–43764 (2012).
9. Feld, G. K., Brown, M. J. & Krantz, B. A. Ratcheting up protein translocation with anthrax toxin. *Protein Sci.* **21,** 606–624 (2012).
10. Petosa, C., Collier, R. J., Klimpel, K. R., Leppla, S. H. & Liddington, R. C. Crystal structure of the anthrax toxin protective antigen. *Nature* **385,** 833–838 (1997).
11. Santelli, E., Bankston, L. A., Leppla, S. H. & Liddington, R. C. Crystal structure of a complex between anthrax toxin and its host cell receptor. *Nature* **430,** 905–908 (2004).
12. Lacy, D. B., Wigelsworth, D. J., Melnyk, R. A., Harrison, S. C. & Collier, R. J. Structure of heptameric protective antigen bound to an anthrax toxin receptor: a role for receptor in pH-dependent pore formation. *Proc. Natl Acad. Sci. USA* **101,** 13147–13151 (2004).
13. Kintzer, A. F. *et al.* The protective antigen component of anthrax toxin forms functional octameric complexes. *J. Mol. Biol.* **392,** 614–629 (2009).
14. Feld, G. K. *et al.* Structural basis for the unfolding of anthrax lethal factor by protective antigen oligomers. *Nature Struct. Mol. Biol.* **17,** 1383–1390 (2010).

15. Vernier, G. *et al.* Solubilization and characterization of the anthrax toxin pore in detergent micelles. *Protein Sci.* **18,** 1882–1895 (2009).
16. Sehnal, D. *et al.* MOLE 2.0: advanced approach for analysis of biomacromolecular channels. *J Cheminform.* **5,** 39 (2013).
17. Ziv, G., Haran, G. & Thirumalai, D. Ribosome exit tunnel can entropically stabilize alpha-helices. *Proc. Natl Acad. Sci. USA* **102,** 18956–18961 (2005).
18. Voss, N. R., Gerstein, M., Steitz, T. A. & Moore, P. B. The geometry of the ribosomal polypeptide exit tunnel. *J. Mol. Biol.* **360,** 893–906 (2006).
19. Killian, J. A. & von Heijne, G. How proteins adapt to a membrane-water interface. *Trends Biochem. Sci.* **25,** 429–434 (2000).
20. Wang, J., Vernier, G., Fischer, A. & Collier, R. J. Functions of phenylalanine residues within the beta-barrel stem of the anthrax toxin pore. *PLoS ONE* **4,** e6280 (2009).
21. Song, L. *et al.* Structure of staphylococcal α-hemolysin, a heptameric transmembrane pore. *Science* **274,** 1859–1866 (1996).
22. De, S. & Olson, R. Crystal structure of the *Vibrio cholerae* cytolysin heptamer reveals common features among disparate pore-forming toxins. *Proc. Natl Acad. Sci. USA* **108,** 7385–7390 (2011).
23. Sellman, B. R., Nassi, S. & Collier, R. J. Point mutations in anthrax protective antigen that block translocation. *J. Biol. Chem.* **276,** 8371–8376 (2001).
24. Sellman, B. R., Mourez, M. & Collier, R. J. Dominant-negative mutants of a toxin subunit: an approach to therapy of anthrax. *Science* **292,** 695–697 (2001).
25. Mourez, M. *et al.* Mapping dominant-negative mutations of anthrax protective antigen by scanning mutagenesis. *Proc. Natl Acad. Sci. USA* **100,** 13803–13808 (2003).
26. Melnyk, R. A. & Collier, R. J. A loop network within the anthrax toxin pore positions the phenylalanine clamp in an active conformation. *Proc. Natl Acad. Sci. USA* **103,** 9802–9807 (2006).
27. Ballester, P. & Biros, S. M. in *The Importance of Pi-Interactions in Crystal Engineering* 79–107 (John Wiley, 2012).
28. Goyal, P. *et al.* Structural and mechanistic insights into the bacterial amyloid secretion channel CsgG. *Nature* **516,** 250–253 (2014).
29. Finkelstein, A. Proton-coupled protein transport through the anthrax toxin channel. *Phil. Trans. R. Soc. B* **364,** 209–215 (2009).
30. Kintzer, A. F. Tang, Il, Schawel, A. K., Brown, M. J. & Krantz, B. A. Anthrax toxin protective antigen integrates poly-gamma-D-glutamate and pH signals to sense the optimal environment for channel formation. *Proc. Natl Acad. Sci. USA* **109,** 18378–18383 (2012).

Supplementary Information is available in the online version of the paper.

Author Contributions J.J. designed and performed the experiments, analysed data, and wrote the paper; Z.H.Z. initialized and supervised the research, analysed data, and wrote the paper. B.L.P. and R.J.C. analysed data and wrote the paper.

METHODS

No statistical methods were used to predetermine sample size.

Preparation of PA prepores. PA_{63} prepores were prepared following the described procedures[31].

EM sample preparation and data acquisition. For negative-stain EM, 2 µl of 0.1% polylysine solution (Polysciences) was first applied to a glow-discharged grid covered with carbon film and then removed by blotting with filter paper in 2 min. The polylysine treatment produced different orientations of particles on EM grids[32], therefore overcoming the problem of preferred orientation for the PA pore. Immediately after removal of polylysine, 2 µl of PA prepore (~50 µg ml^{-1}) was applied to the grid and incubated for 1 min. The grid was then washed with the high-pH buffer (50 mM HEPES, 50 mM NaCl, pH 8.0) twice followed by two washes with the low-pH buffer (50 mM NaOAc, pH 5.0, 0.05% Igepal CA-630) to induce the conversion of prepore to pore. After removal of excess buffer, the grid was stained with 0.8% (w/v) uranyl formate.

For cryoEM, Quantifoil R1.2/1.3 holey grids were covered with a thin layer of continuous carbon film one day before use. The procedure for pore induction on cryoEM grids followed the same procedure for the negative-stain EM except that the last step of staining was not used. About 1.5 µl of low-pH buffer was left on the grids before they were transferred into an FEI Vitrobot Mark IV. The grids were then blotted and flash-frozen in liquid ethane in the Vitrobot at 100% humidity. The frozen grids were stored in liquid nitrogen before use.

Negative-stain EM micrographs were acquired with Leginon automation software[33,34] and a TIETZ F415MP 16-megapixel CCD camera at ×68,027 magnification in an FEI Tecnai F20 electron microscope operated at 200 kV. The micrographs were saved by 2× binning to yield a pixel size of 4.4 Å.

Frozen-hydrated cryoEM grids were loaded into an FEI Titan Krios electron microscope operated at 300 kV for automated image acquisition with Leginon. CryoEM micrographs were recorded on a Gatan K2 Summit direct electron detection camera using the electron counting mode at ×22,500 nominal magnification (calibrated pixel size of 1.28 Å on the sample level) and defocus values ranging from −1.8 to −5.1 µm. The dose rate on the camera was set to about 8 electrons per pixel per second. The total exposure time was 8 s and fractionated into 32 frames of subimages with 0.25 s exposure time for each frame. Frame images were aligned and averaged for correction of beam-induced drift using the GPU-accelerated program from Y. Cheng's laboratory[35]. The average images from all frames were used for defocus determination and particle picking, and those from the first 16 frames (corresponding to about 20 electrons per square ångström total dose on sample) were used for two- and three-dimensional image classifications. In total, 12,416 micrographs were taken in a continuous session. The best 7,062 micrographs were selected for the following in-depth data processing.

Image processing. For negative-stain EM single particle reconstruction, 140,775 particles were picked from 1,115 negative-stain EM micrographs using the batchboxer program of EMAN[36]. Particles were windowed out in 96 pixels × 96 pixels. The defocus value of each micrograph was determined by CTFFIND[37] and particles were corrected for contrast transfer function (CTF) by phase-flipping with the corresponding defocus and astigmatism values using Bsoft[38]. An initial model was generated using the startcsym program of EMAN. The refinement was then performed with sevenfold symmetry using EMAN.

For cryoEM single particle reconstruction, 21,200 particles (256 pixels × 256 pixels) were initially picked by hand from 1,928 micrographs and subjected to auto-refinement by RELION[39,40] using the negative-stain EM map obtained above as the initial model. The resulting cryoEM map (approximately 4-Å resolution) was used to generate projections that were then served as templates to pick 259,719 particles from all of the 7,062 micrographs using the batchboxer of EMAN. In our procedure, the defocus values of the micrographs were determined by CTFFIND and particles were corrected for CTF by phase-flipping using Bsoft. The particles were processed with two- and three-dimensional classifications using the recommended procedures of RELION (http://www2.mrc-lmb.cam.ac.uk/relion/index.php/Recommended_procedures). Two-dimensional class averages and three-dimensional class reconstructions were inspected and those without high-resolution and interpretable features were considered as 'bad' classes. Particles contributing to the bad classes were discarded. The remaining 60,455 particles were selected for the final structure refinement. The C7 symmetry was applied throughout the three-dimensional classification and three-dimensional auto-refinement.

To maximize usable signals from the frame images acquired with the K2 Summit camera, we used the resolution and dose-dependent model of radiation damage recently introduced in RELION-1.3 in the following steps[41]. First, the particle images averaged from all 32 frames with whole-image drift correction were used for a preliminary three-dimensional auto-refinement. Second, particle images from individual frames were used to calculate translational alignments for the particle-based drift correction. A running average of seven frames, a standard deviation of one

pixel, and fitting of linear tracks through the translations for all running averages were used for the optimal translational alignment following the suggested protocol of RELION. Last, particle images from frame 3 to frame 27 (~30 electrons per square ångström total dose on sample) were translated using the above optimal alignment and weighted with different B-factors as estimated from the single-frame reconstructions to generate optimal 'shiny' average images. Application of this procedure to the above selected particles yielded 60,455 'shiny' particles.

These 'shiny' particles were then subjected to three-dimensional auto-refinement in RELION to generate the final cryoEM map. RELION post-processing with a soft auto-mask[42] estimated a resolution of 2.9 Å by the 'gold standard' Fourier shell correlation (FSC) at 0.143 criterion and a B-factor of −95 Å^2, and the post-processing without any mask reported a resolution of 3.3 Å. The accuracies of rotation and translation reported by RELION three-dimensional auto-refinement were 1.67° and 1.01 Å. For visualization and atomic model building, the cryoEM map was sharpened and low-pass filtered by RELION post-processing using the above-mentioned B-factor and resolution. Local resolution was calculated by ResMap[43] using the two cryoEM maps independently refined from halves of data.

Three-dimensional classification and auto-refinement also identified a subset of 21,632 particles that led to a cryoEM map at 3.6-Å resolution, which was in the pore state but lacked the density corresponding to the 14-stranded β-barrel: that is, it only had the corolla and calyx of the PA pore.

Atomic model building and refinement. *De novo* atomic model building of the PA pore except its domain 4 was performed on the cryoEM map at 2.9-Å resolution using Coot[44]. The coarse model was then refined using PHENIX in a pseudo-crystallographic manner[45]. Note this procedure only improved the atomic model and did not modify the cryoEM map. Briefly, the cryoEM map was put into an artificial crystal lattice to calculate its structure factor using the em_map_to_hkl.inp utility program in CNS[46]. The amplitudes and phases of the structure factor were used as pseudo-experimental diffraction data for model refinement in PHENIX. The restraints of Ramachandran, secondary structure, and non-crystallographic symmetry were used in the refinement.

The cryoEM maps and atomic models were visualized using UCSF Chimera[47] or PyMOL[48]. The available crystal structures of PA_{83} monomer (for example, PDB accession numbers 1ACC and 3TEW) and PA_{63} heptameric prepore (PDB accession number 1TZO) are highly similar to each other; therefore 3TEW, which has the highest resolution among them, was used for structural comparison with our cryoEM structure of the PA pore in most situations and 1TZO was used when the inter-protomer interaction or domain movement were considered.

31. Wigelsworth, D. J. *et al.* Binding stoichiometry and kinetics of the interaction of a human anthrax toxin receptor, CMG2, with protective antigen. *J. Biol. Chem.* **279,** 23349–23356 (2004).
32. Ortega, J., Singh, S. K., Ishikawa, T., Maurizi, M. R. & Steven, A. C. Visualization of substrate binding and translocation by the ATP-dependent protease, ClpXP. *Mol. Cell* **6,** 1515–1521 (2000).
33. Suloway, C. *et al.* Automated molecular microscopy: the new Leginon system. *J. Struct. Biol.* **151,** 41–60 (2005).
34. Suloway, C. *et al.* Fully automated, sequential tilt-series acquisition with Leginon. *J. Struct. Biol.* **167,** 11–18 (2009).
35. Li, X. *et al.* Electron counting and beam-induced motion correction enable near-atomic-resolution single-particle cryo-EM. *Nature Methods* **10,** 584–590 (2013).
36. Ludtke, S. J., Baldwin, P. R. & Chiu, W. EMAN: semiautomated software for high-resolution single-particle reconstructions. *J. Struct. Biol.* **128,** 82–97 (1999).
37. Mindell, J. A. & Grigorieff, N. Accurate determination of local defocus and specimen tilt in electron microscopy. *J. Struct. Biol.* **142,** 334–347 (2003).
38. Heymann, J. B. Bsoft: image and molecular processing in electron microscopy. *J. Struct. Biol.* **133,** 156–169 (2001).
39. Scheres, S. H. RELION: implementation of a Bayesian approach to cryo-EM structure determination. *J. Struct. Biol.* **180,** 519–530 (2012).
40. Scheres, S. H. A Bayesian view on cryo-EM structure determination. *J. Mol. Biol.* **415,** 406–418 (2012).
41. Scheres, S. H. Beam-induced motion correction for sub-megadalton cryo-EM particles. *eLife* **3,** e03665 (2014).
42. Amunts, A. *et al.* Structure of the yeast mitochondrial large ribosomal subunit. *Science* **343,** 1485–1489 (2014).
43. Swint-Kruse, L. & Brown, C. S. Resmap: automated representation of macromolecular interfaces as two-dimensional networks. *Bioinformatics* **21,** 3327–3328 (2005).
44. Emsley, P. & Cowtan, K. Coot: model-building tools for molecular graphics. *Acta Crystallogr. D* **60,** 2126–2132 (2004).
45. Adams, P. D. *et al.* PHENIX: a comprehensive Python-based system for macromolecular structure solution. *Acta Crystallogr. D* **66,** 213–221 (2010).
46. Brunger, A. T. *et al.* Crystallography & NMR system: a new software suite for macromolecular structure determination. *Acta Crystallogr. D* **54,** 905–921 (1998).
47. Pettersen, E. F. *et al.* UCSF Chimera—a visualization system for exploratory research and analysis. *J. Comput. Chem.* **25,** 1605–1612 (2004).
48. Schrodinger, LLC. The PyMOL Molecular Graphics System, v.1.7.2 (2014).
49. Krissinel, E. & Henrick, K. Inference of macromolecular assemblies from crystalline state. *J. Mol. Biol.* **372,** 774–797 (2007).
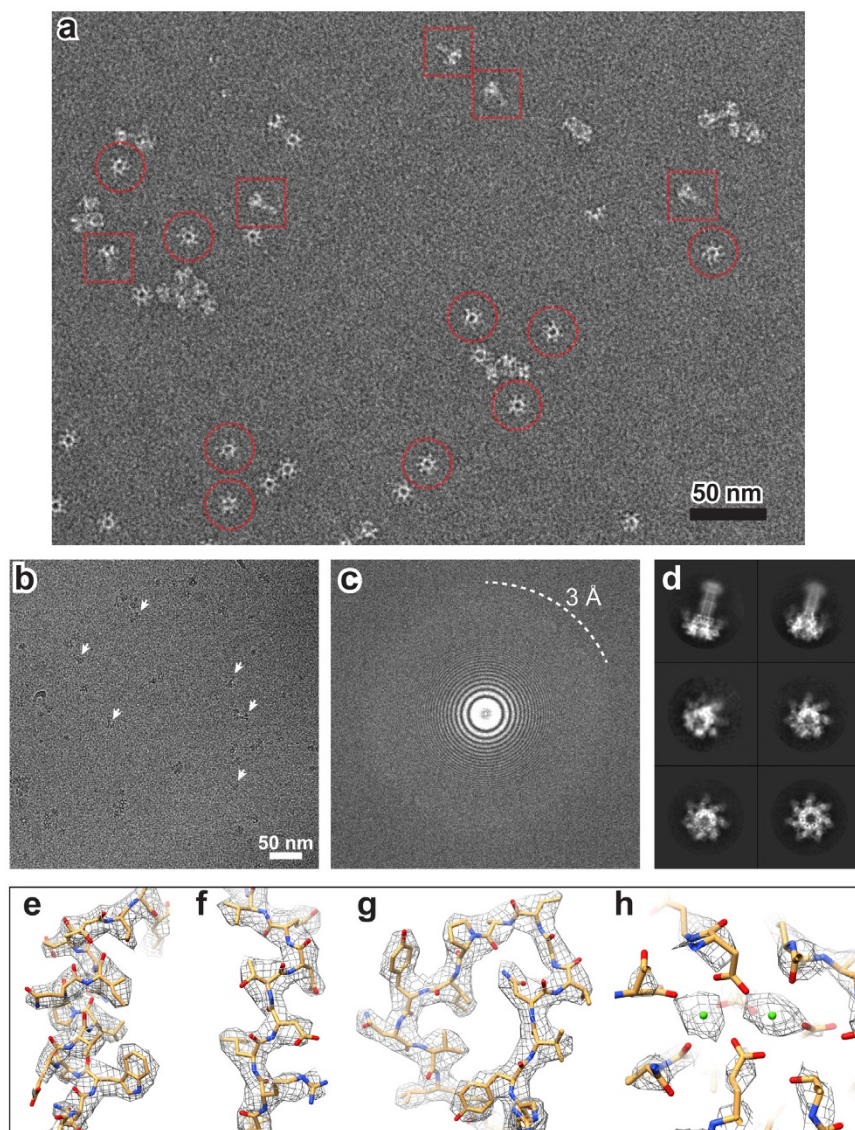
**Extended Data Figure 1 | Negative-stain and cryoEM of the PA pore.**
a, Negative-stain EM micrograph of PA pore particles. Some representative top-view and side-view particles are selected with circles and squares, respectively. b, A full-size drift-corrected cryoEM micrograph of 3,710 pixels × 3,710 pixels of PA pore particles acquired from a Gatan K2 Summit direct electron detection camera, at 300 kV accelerating voltage, −2.7 μm defocus, and a total dose of 39 electrons per square ångström. Some representative side-view particles of PA pore are indicated by arrows. c, Power spectrum of the cryoEM micrograph in b. d, Representative cryoEM two-dimensional class averages of particles at different orientations. e–h, Superimposition of representative regions of the cryoEM map (mesh) with the atomic model (stick), including α-helix (e), β-strand (f), loop (g), and Ca^{2+} ions (green spheres in h).
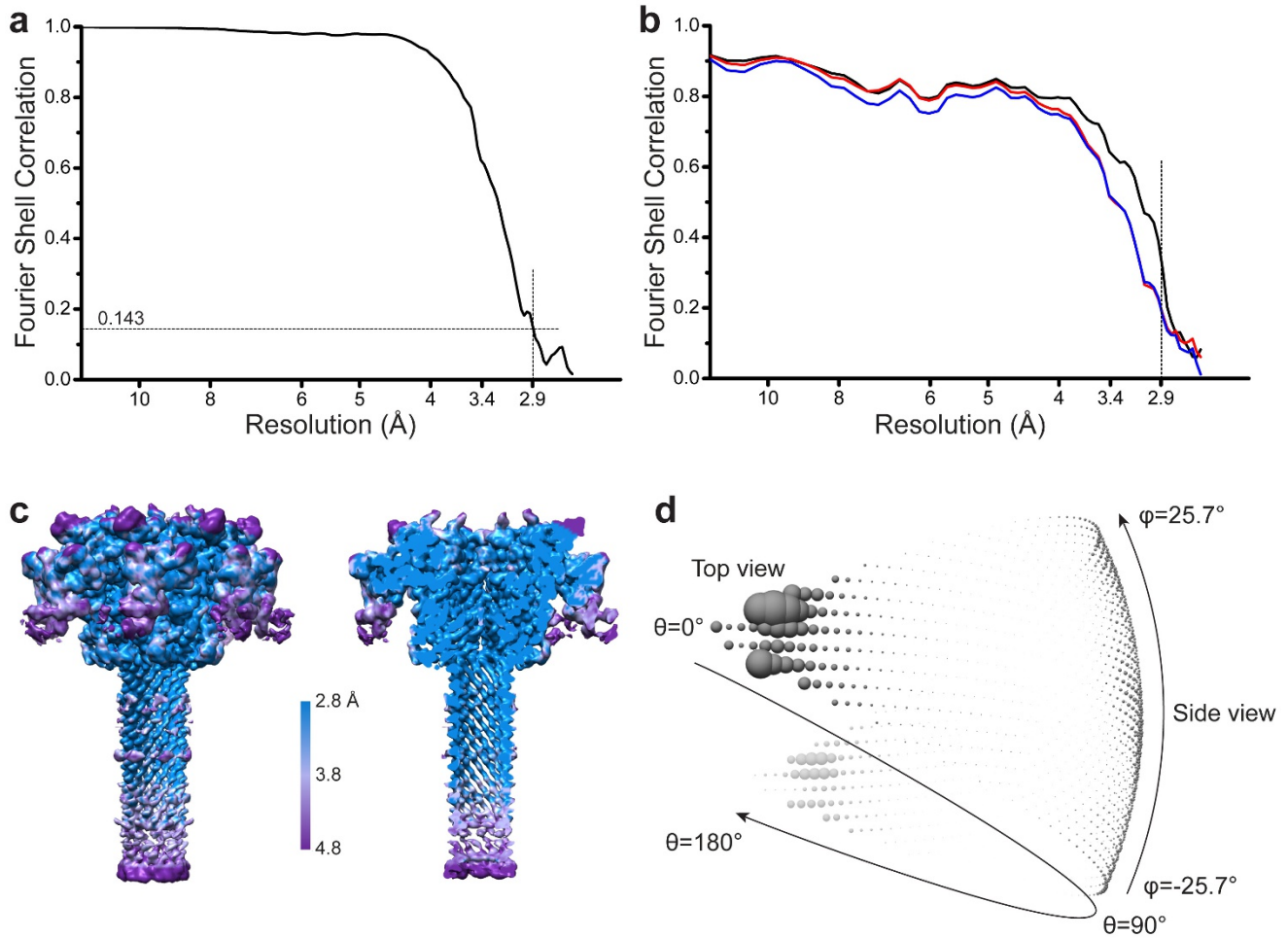
Extended Data Figure 2 | Resolution estimation of the cryoEM single particle reconstruction of the PA pore. **a**, 'Gold standard' FSC between two independently refined maps with an auto-mask that was corrected by phase randomization. The resolution was estimated by the 'gold standard' FSC at 0.143 criterion[42]. **b**, FSC of the final atomic model versus the final cryoEM map (black); of a model refined in the first of the two independent maps used for the 'gold standard' FSC versus the same map (red) and versus the second independent map (blue). **c**, Surface view and cut-through view of the unsharpened cryoEM map coloured by local resolution estimated by ResMap[43]. **d**, Euler angle distribution of all particles used for the final three-dimensional reconstruction.
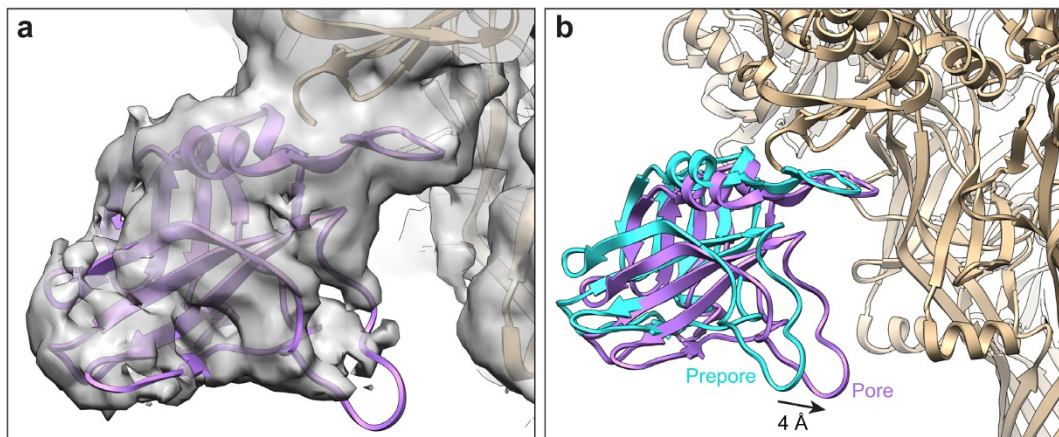
Extended Data Figure 3 | Fitting of domain 4 into the cryoEM map of PA pore. a, The crystal structure of domain 4 (purple ribbons) from PA prepore (PDB accession number 1TZO) fits the cryoEM map (grey surface) of PA pore with a good agreement (cross-correlation coefficient: 0.91). **b,** Translocation of domain 4 during the prepore to pore conversion. Domain 4 is shifted inwards as a rigid-body for 4 Å from the prepore conformation (dark cyan) to the pore conformation (purple).
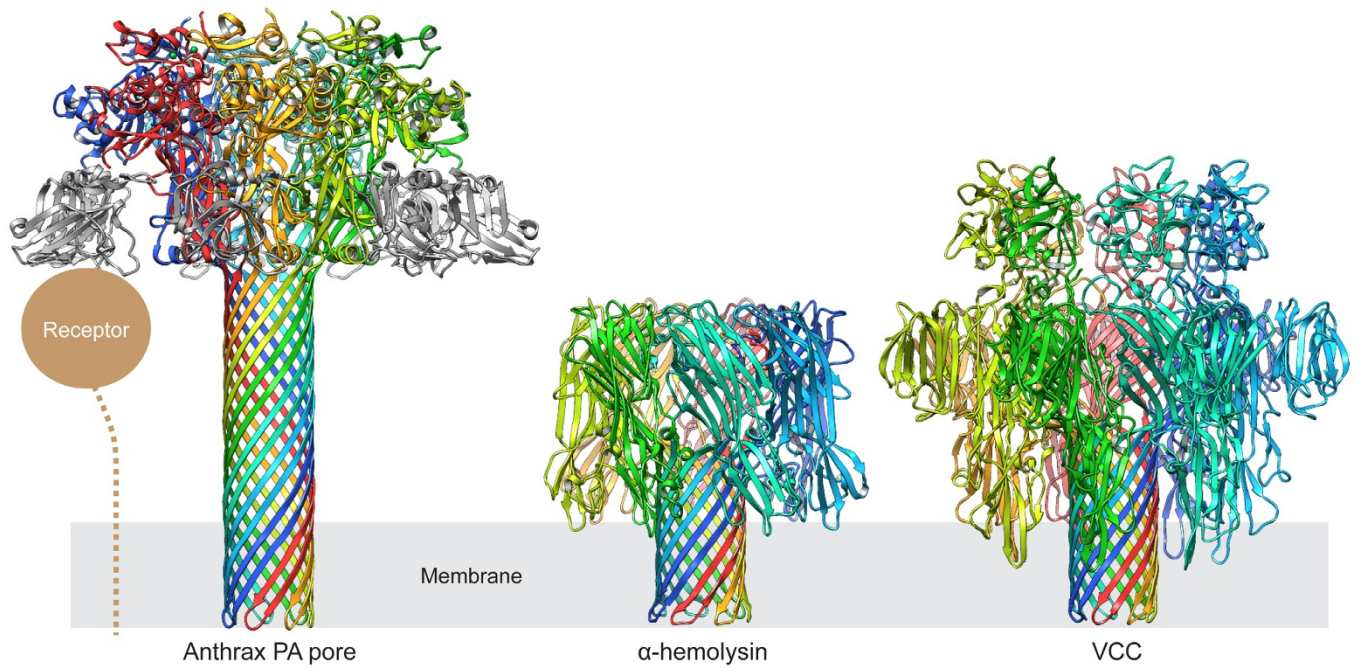
Extended Data Figure 4 | Comparison of the structures of the PA pore, α-haemolysin (PDB accession number 7AHL), and *Vibrio cholerae* cytolysin (PDB accession number 3O44). These three complexes are in their membrane-inserted forms. The approximate position of the lipid bilayer is illustrated with grey shade. The host cell receptor (TEM8 or CMG2) of PA that binds to domain 4 (grey ribbons) is schematically illustrated.
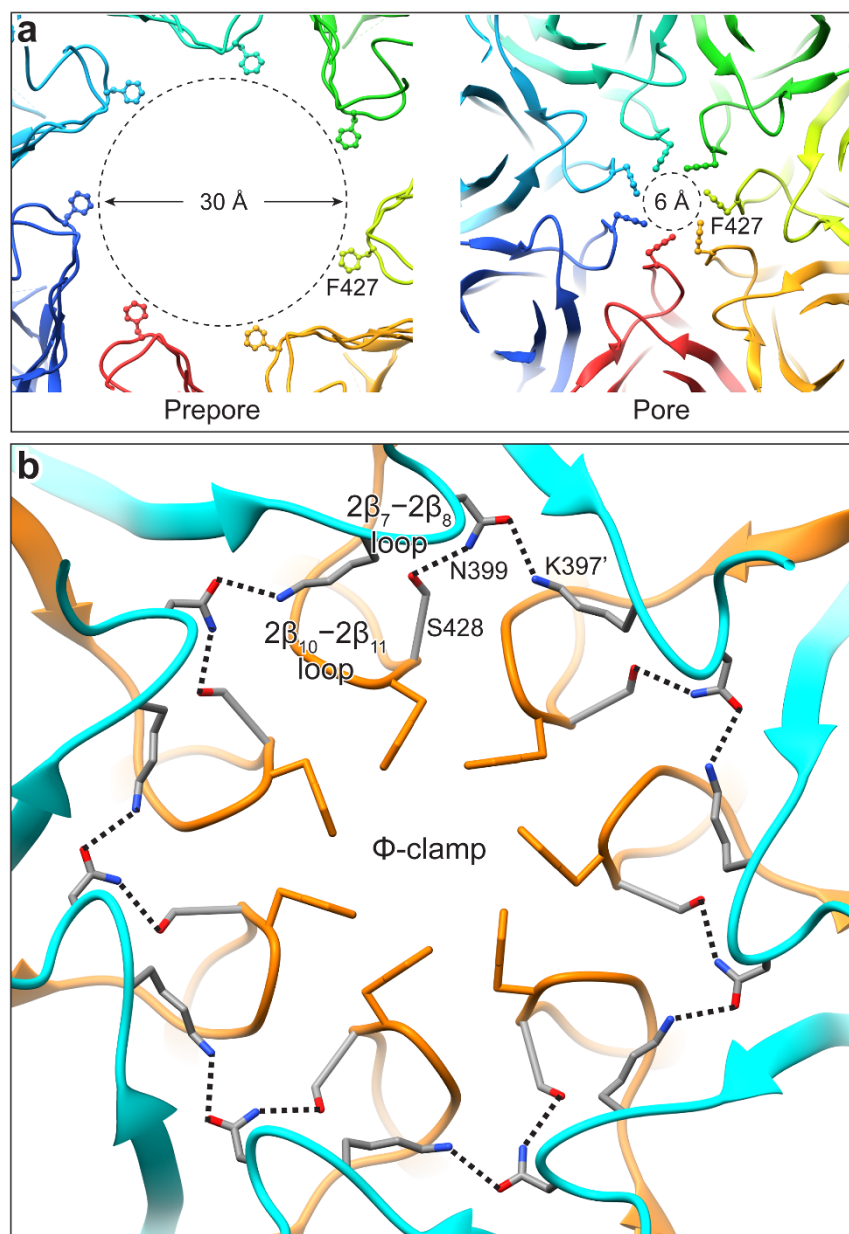
Extended Data Figure 5 | Assembling of the Φ-clamp in the PA pore.
a, Comparison of the Φ-clamp in the PA pore with its corresponding region in the PA prepore. The residues Asp426 and Phe427 missing in the crystal structure of the PA_{63} prepore (PDB accession number 1TZO) are modelled based the crystal structure of the PA_{83} monomer (PDB accession number 1ACC). **b**, Close-up top view of the Φ-clamp region in the PA pore. The $2\beta_7$–$2\beta_8$ and $2\beta_{10}$–$2\beta_{11}$ loops are coloured in cyan and orange, respectively. The hydrogen bonds between Ser428, Asn399, and Lys397′, which form a chain tethering the $2\beta_7$–$2\beta_8$ and $2\beta_{10}$–$2\beta_{11}$ loops together, are depicted with dashed lines.
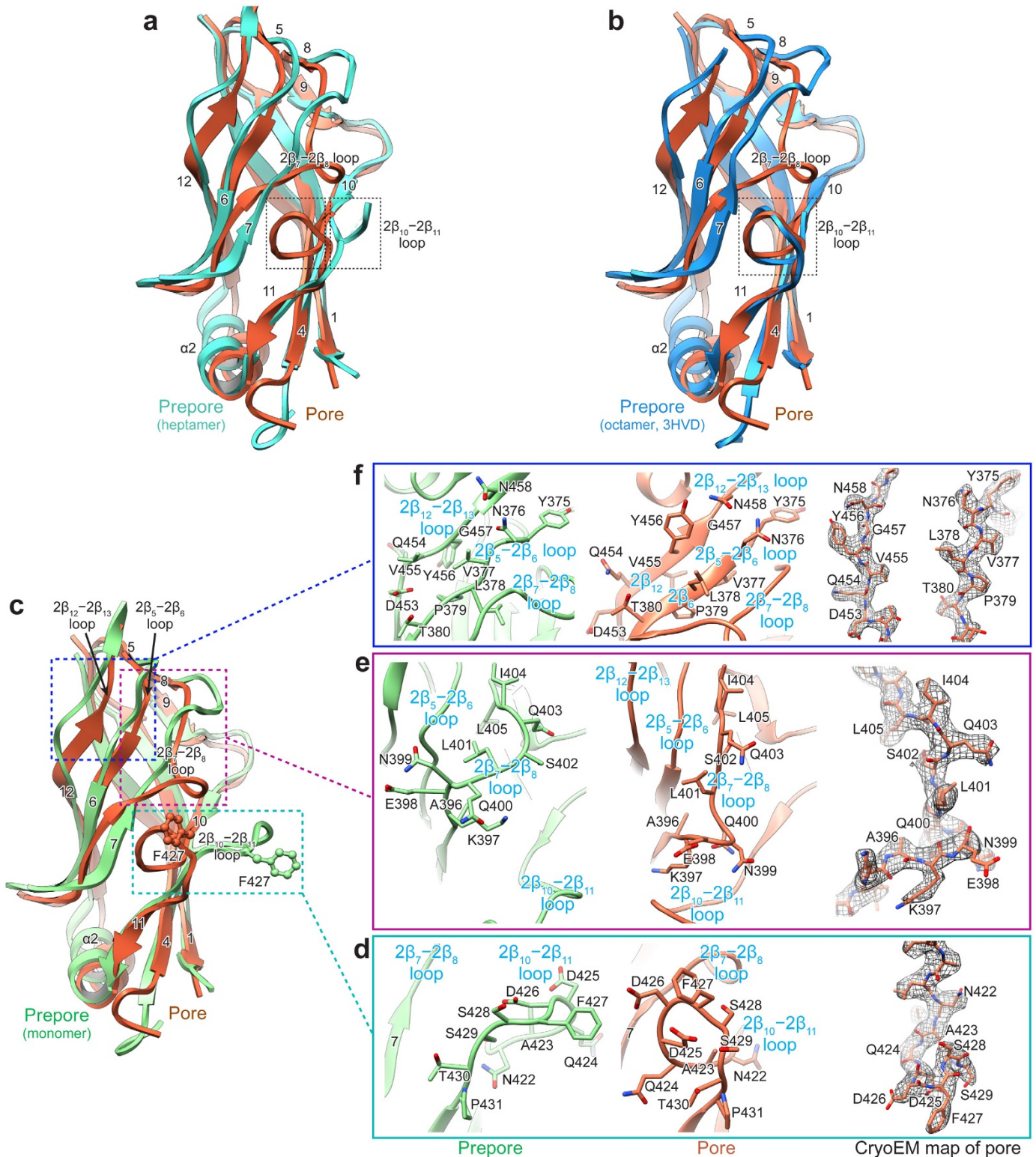
Extended Data Figure 6 | Conformational changes of domain 2c between the PA prepore and the PA pore. a, Superimposition of domains 2c of the PA pore and the crystal structure of the PA heptameric prepore (PDB accession number 1TZO). The dashed boxes highlight the conformational difference of the $2\beta_{10}$–$2\beta_{11}$ loop between these two structures. Residues Asp426 and Phe427 are not solved in the crystal structure of PA prepore because of their flexibility. **b**, Superimposition of domains 2c of the PA pore and the PA octameric prepore (PDB accession number 3HVD). Note the similarity of the $2\beta_{10}$–$2\beta_{11}$ loop (dashed box) between these two structures. **c**, Superimposition of domains 2c of the PA pore and the PA prepore (monomer; PDB accession number 3TEW). **d–f**, Close-up views of the rearrangements of the $2\beta_{10}$–$2\beta_{11}$ loop (**d**), the $2\beta_7$–$2\beta_8$ loop (**e**), and the $2\beta_5$–$2\beta_6$ and $2\beta_{12}$–$2\beta_{13}$ loops (**f**) during the conversion from prepore to pore. Val377 and Leu378 of the $2\beta_5$–$2\beta_6$ loop and Val455 and Tyr456 of the $2\beta_{12}$–$2\beta_{13}$ loop are flipped upside down to obtain the β-strand conformation in the PA pore, leading to an extension of $2\beta_6$ and $2\beta_{12}$ (**f**). CryoEM densities (mesh) corresponding to these loops are displayed to the right of **d–f** with atomic models superimposed, showing unambiguous atomic modelling. The superimpositions of the cryoEM map and the atomic model are shown in views different from the left panels for clarity. The conformational changes of these loops result in a more compact domain 2c with a decrease of 567 Å^2 in its surface area.
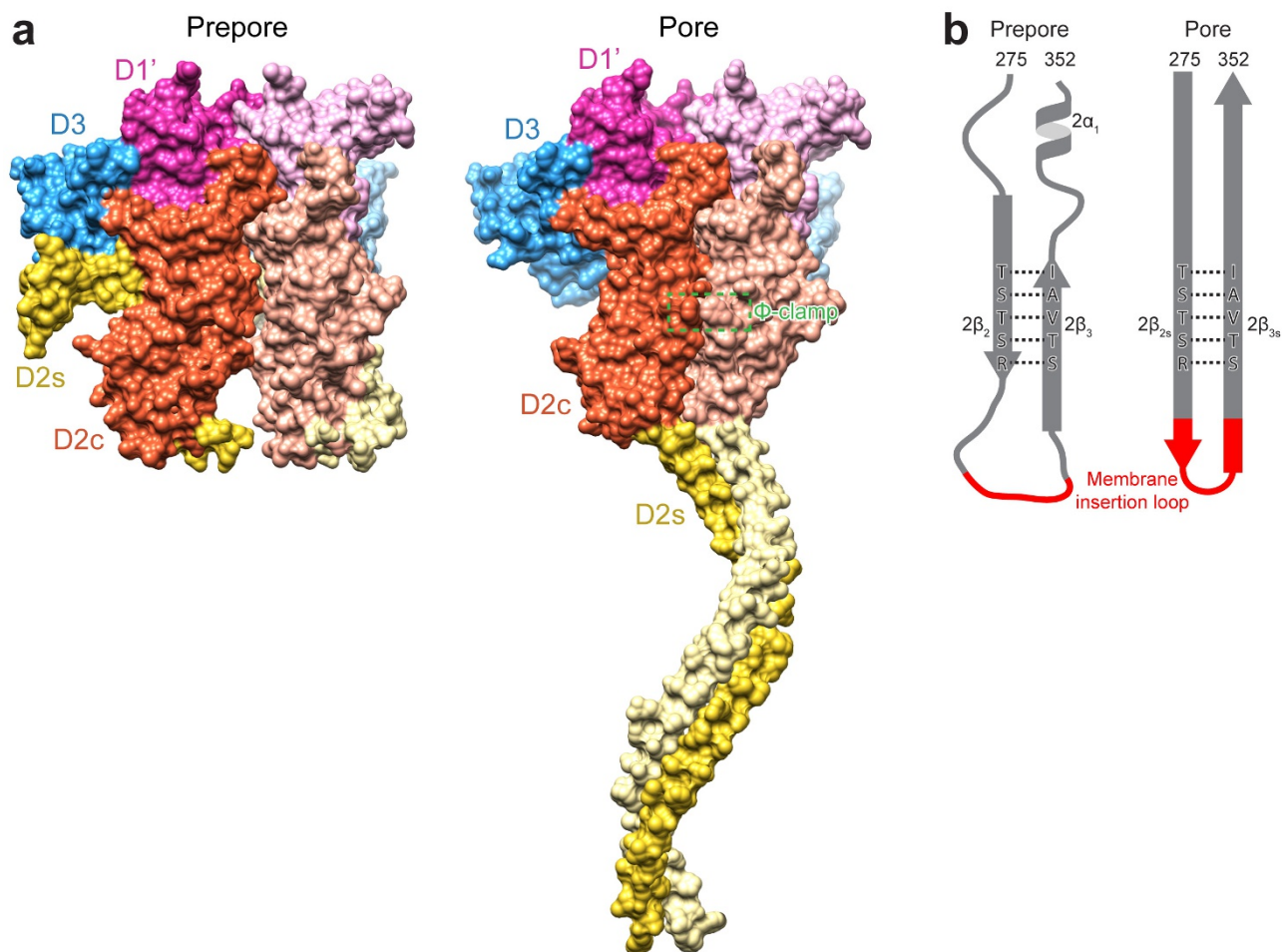
Extended Data Figure 7 | Compact assembly of the PA pore. a, Surface views of two neighbouring protomers (the same domains in the two protomors are in different shades of the same colours) of the PA pore and the PA prepore (PDB accession number 1TZO) visualized from inside the PA heptamer. Domains 1′, 2c, 2s, and 3 are coloured differently and domain 4 is not shown. The inter-protomer interface in the PA prepore is largely formed by domains 1′ and 3, and domain 2 only contributes to this interface by its membrane insertion loop and carboxy (C)-terminal region ($2\beta_{13}$, $2\beta_{14}$, and $2\alpha_3$). In the PA pore, the convergence of domain 2c creates an inter-protomer interface without any gap, with an increase of interface area on domain 2c from 1,247 Å^2 of the PA prepore to 2,106 Å^2 of the PA pore as calculated using PISA[49] (http://www.ebi.ac.uk/pdbe/pisa/). Additionally, formation of the β-barrel also leads to extensive contacts, creating a new interface area of 1,195 Å^2 between two protomers. **b,** Schematic of the conversion of $2\beta_2$, $2\beta_3$, $2\alpha_1$, and the membrane insertion loop of the PA prepore to $2\beta_{2s}$ and $2\beta_{3s}$ of the PA pore. Hydrogen bonds between $2\beta_2$ and $2\beta_3$, which are depicted with dashed lines, are maintained during the conversion. By contrast, $2\alpha_1$ and the connecting loops have to be fully unfolded and converted into β-strands that collectively assemble the β-barrel of the PA pore. Although the detailed events of β-barrel formation are not yet clear, it is likely that assembly starts from the top in a zipper-like manner. A favourable scenario is that the convergence of domain 2c would place the top ends of the β-strands close to each other to form a short β-barrel, which could extend by pulling more residues together via formation of ordered hydrogen bonds until it reaches the bottom end. It is less favourable that the assembly starts from other regions because disordered hydrogen bonds and hydrophobic interactions could generate enormous non-productive, possibly irreversible pairings between strands.
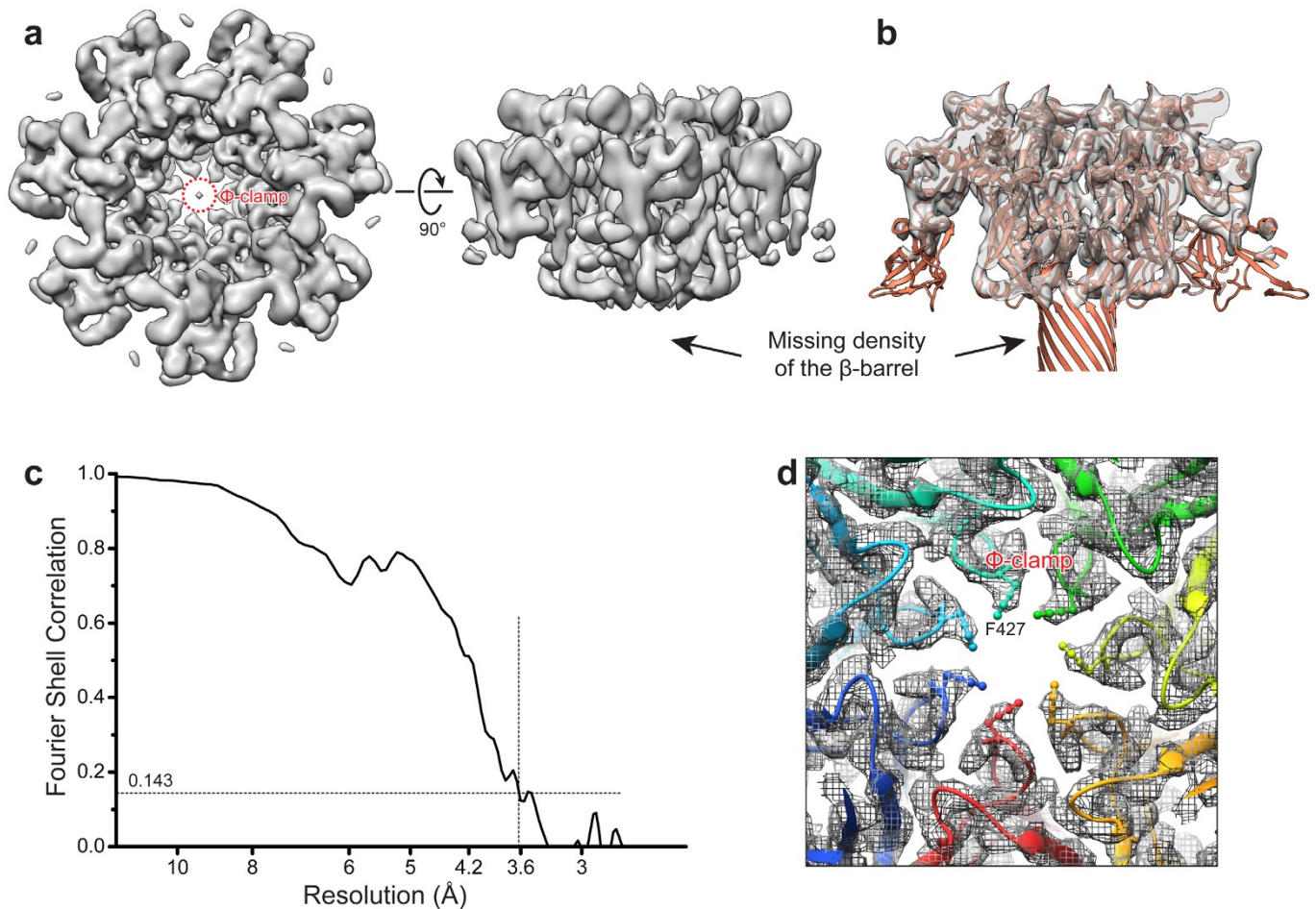
Extended Data Figure 8 | CryoEM single-particle reconstruction of a subset of particles lacking the 14-stranded β-barrel. **a**, Surface views of the cryoEM map lacking the β-barrel. The map is unsharpened and has a resolution of 3.6 Å. **b**, Cross-section side view of superimposition of the unsharpened cryoEM map with the atomic model of the intact PA pore, showing the cryoEM map has the same conformation as the PA pore except for the absence of the 14-stranded β-barrel. **c**, 'Gold standard' FSC (with an auto-mask that was corrected by phase randomization) between two independently refined maps. **d**, Top view of the Φ-clamp region of the cryoEM map (mesh) lacking the β-barrel superimposed with the atomic model of the PA pore (ribbons), showing correct assembling of the Φ-clamp in the cryoEM map.

Extended Data Table 1 | Data collection and structure refinement statistics

Data Collection	
Particles	60,455
Pixel size (Å)	1.28
Defocus range (µm)	-1.8 to -5.1
Voltage (kV)	300
Total electron dose	39 $e^-/\text{Å}^2$
Electron dose used in the final reconstruction	30 $e^-/\text{Å}^2$
Refinement	
Resolution (Å)	2.9
Map sharpening B-factor (Å^2)	-95
Average B-factor (Å^2)	81
R.m.s deviations	
Bond lengths (Å)	0.009
Bond angles (°)	1.083